

pubs.acs.org/acscatalysis Research Article

# Computationally Guided Design to Accelerate Discovery of Doped $\beta$ -Mo<sub>2</sub>C Catalysts toward Hydrogen Evolution Reaction

Timothy T. Yang, Anqi Wang, Stephen D. House, Judith Yang, Jung-Kun Lee,\* and Wissam A. Saidi\*



Cite This: ACS Catal. 2022, 12, 11791–11800



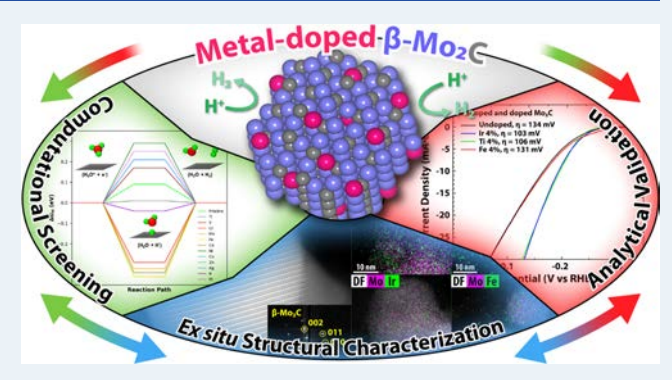
**ACCESS** 

III Metrics & More

Article Recommendations

s Supporting Information

**ABSTRACT:** Low-cost molybdenum carbides have shown a rapid increase in their efficiency toward catalyzing the hydrogen evolution reaction (HER) owing to their structural flexibility for metal doping and nanostructure engineering. Herein, we employ first-principles quantum mechanical calculations in conjunction with thermodynamic analysis to shortlist ideal single-metal dopants that improve HER catalytic activity of β-Mo<sub>2</sub>C. We show that Ir or Ti substitutional doping at the Mo sites of β-Mo<sub>2</sub>C introduces thermoneutral hydrogen adsorption sites for HER, while the other elements in the first-row transition metals and Pt and Ag are not effective dopants for HER. To validate the computational results, we employ a microwave-assisted solvothermal method to synthesize metal-doped β-Mo<sub>2</sub>C nanoparticles (NPs) and assess



their HER performance and structure using a suite of electrochemical and ex situ structural characterizations. From cyclic voltammetry, we find that the HER onset voltage of pristine  $\beta$ -Mo<sub>2</sub>C NPs decreases by more than 20% through impurity doping with Ti or Ir and is accompanied by a discernable increase in exchange current density. Transmission electron microscopy (TEM), high-angle annular dark-field scanning TEM (HAADF-STEM), and energy-dispersive X-ray spectroscopy (EDS) confirm that such an increase in HER activities originates from impurity doping and is not due to morphological or phase changes of the catalyst. The present study demonstrates that a combined and synergistic experimental and computational approach is indispensable to uncover the atomistic origins of catalytic activity and provide a rational design of the catalyst.

KEYWORDS: catalyst design, hydrogen evolution reaction, first-principles, microwave synthesis, transmission electron microscopy

## ■ INTRODUCTION

Green hydrogen produced from electrolysis, the electrochemical process of splitting water using electricity generated from solar or wind power, is a key enabler of the global transition to sustainability and net-zero emission by 2050.1 Hydrogen has high potential to be stored cost-effectively and thus can support the integration of different renewables in the electric grid. Also, hydrogen can be utilized to decarbonize a range of energy sectors, such as iron and steel, chemical, and cement production, that are proven difficult to reduce emissions.<sup>3</sup> One of the central challenges in the production of hydrogen from water electrolysis is the use of expensive precious metals to catalyze the hydrogen evolution reaction (HER)—the critical process in water splitting to generate hydrogen via combining electrons and protons. This is emphasized in a 2020 workshop on Advances, Challenges, and Long-Term Opportunities in Electrochemistry. Among the newly investigated HER catalysts, low-cost molybdenum carbides (Mo<sub>v</sub>C) are reported to have high HER activities.<sup>5-7</sup>

Mo<sub>2</sub>C can be stabilized into several phases including  $\alpha$ -Mo<sub>2</sub>C,  $\beta$ -Mo<sub>2</sub>C,  $\alpha$ -MoC,  $\gamma$ -MoC,  $\delta$ -MoC, and  $\eta$ -MoC. Among these phases,  $\beta$ -Mo<sub>2</sub>C is found to be the most

catalytically active phase. <sup>7,11</sup> In a previous study, we showed that the active sites of  $\beta$ -Mo<sub>2</sub>C originate from the (011) surface that exposes Mo–C atoms, as it has low surface energy and can bind hydrogen optimally. <sup>12</sup> In the last few years, considerable attention has been devoted to further improving the HER efficiency of Mo<sub>y</sub>C catalysts via a complex nanostructuring approach that involves a hybrid of several mechanisms. For example, Wu and collaborators synthesized  $\eta$ -MoC<sub>1-x</sub> via a confined *in situ* carburization process of Mobased polyoxometalates and Cu-based metal—organic frameworks and showed that the composite system exhibits excellent HER activity. <sup>13</sup> Notably, incorporation of carbon supports—such as carbon nanotubes, <sup>14–16</sup> graphene (GA), <sup>17–23</sup> reduced GA oxide (RGO), <sup>21,24</sup> or nitrogen-doped carbon nanostructues <sup>25–27</sup>—is found to appreciably enhance HER for  $\beta$ -

Received: July 1, 2022 Revised: August 30, 2022



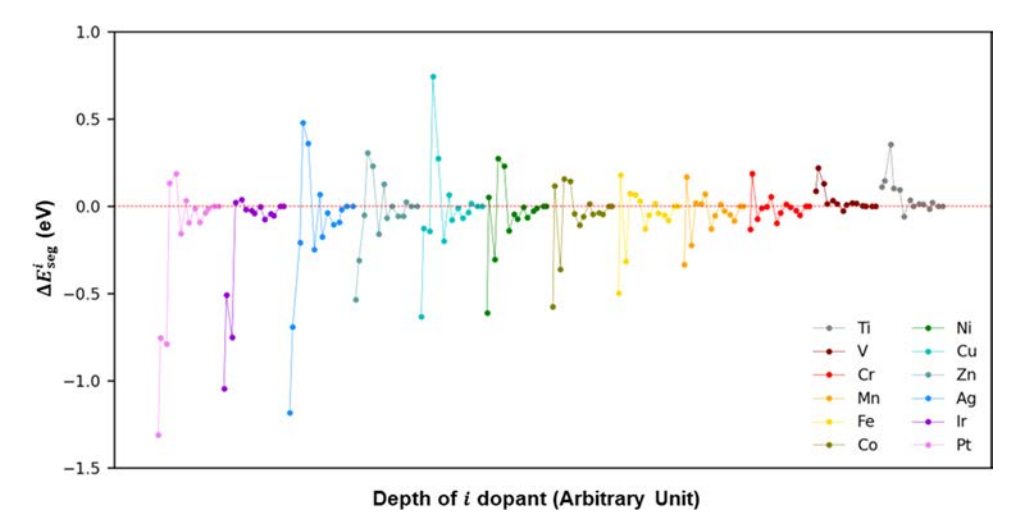


**Figure 1.** Segregation energy  $\Delta E_{\text{seg}}^i$  in eV. For each metal-doped surface, doping layer i increases from left to right with i = 1 corresponding to the top exposed surface layer and i = 7 for the bulklike layer. Each two consecutive values correspond to the same i with slightly different depths. Odd (even) numbers correspond to layers that are composed of Mo–C (Mo), as shown in Figure 2b.

Mo<sub>2</sub>C and δ-MoC. <sup>17,19,20</sup> Nonmetallic (P, <sup>28,29</sup> N, <sup>26,30,31</sup> and S<sup>32,33</sup>) and metal (Fe<sup>38</sup> and Co<sup>39</sup>) dopants have also been reported to improve HER activity. In addition, coupling of Mo<sub>y</sub>C phases<sup>34–39</sup> or MoS<sub>2</sub><sup>40–43</sup> also has been shown to improve activity. Recently, Yang and Saidi showed that nanostructuring creates HER-active sites not only on Mo<sub>y</sub>C but also on the supports due to the modification of the electronic structure of the support through the interactions with Mo<sub>y</sub>C. <sup>44</sup>

While it has been widely observed that heteroatom doping into Mo<sub>v</sub>C enhances HER activity, there is inconsistency across studies. 45,46 Leonard's and Wang's groups observed an insignificant improvement in the HER overpotential of  $Mo_2C$  with Fe doping  $^{45,47}$  (300–400 mV at  $^{10}$  mA/cm<sup>2</sup>); however, Li's group reported a much lower overpotential of 150 mV at 10 mA/cm<sup>2.46</sup> In addition, the reported exchange currents between Fe-, Co-, Ni-, and Cu-doped Mo<sub>2</sub>C are similar with differences of less than  $1.7 \times 10^{-2}$  mA/cm<sup>2</sup>, <sup>47</sup> while we show that the corresponding computed hydrogen adsorption free energies differ by 0.4 eV, suggesting a significantly larger difference of up to the fourth order of magnitude in exchange currents according to the volcano trend. 48-50 These controversies underscore the complexity of uncovering the HER mechanisms of the doped structures. For instance, HER enhancements could originate from different mechanisms, such as modulations in the morphology of nanoparticles (NPs), evolution of Mo<sub>v</sub>C phases under electrochemical conditions, or the modifications of catalytic sites under doping. We posit that while it is challenging for a solely experimental or computational approach to discern between the different mechanisms, a combined approach could provide an effective route for untangling the problem, if any, and enable a rational design of the catalyst.

Using *ab initio* thermodynamics in conjunction with density functional theory calculations, we investigate the modulations of the morphology and hydrogen adsorption sites of  $\beta$ -Mo<sub>2</sub>C via doping with first-row transition metals and three precious metals. The main criterion for our investigations focuses on the long-term stability and enhanced HER activity of the new catalyst. We find that all studied dopants are thermodynamically stable on the exposed  $\beta$ -Mo<sub>2</sub>C surface layer, albeit with different tendencies. However, only Ir and Ti dopants are

predicted to introduce optimum HER-active sites on the  $\beta$ -Mo<sub>2</sub>C surface. To validate the computational findings, we synthesize Ir- and Ti-doped  $\beta$ -Mo<sub>2</sub>C NPs using a microwave-assisted solvothermal method. From cyclic voltammetry, we confirm enhanced HER activities on Ti- and Ir-doped  $\beta$ -Mo<sub>2</sub>C, indicated by an overpotential that is 20% less than that of pristine  $\beta$ -Mo<sub>2</sub>C NPs. In addition, the exchange current densities of the Ir- and Ti-doped  $\beta$ -Mo<sub>2</sub>C NPs are, respectively,  $1.78 \times 10^{-4}$  and  $2.24 \times 10^{-4}$  A/cm², which are higher than  $5.37 \times 10^{-5}$  A/cm² for the pristine  $\beta$ -Mo<sub>2</sub>C NPs. Using HAADF-STEM, HRTEM, and EDS, we confirm that the enhanced HER activities on the Ir- and Ti-doped  $\beta$ -Mo<sub>2</sub>C NPs are due to the electronic structure modulations and not due to morphological changes of the catalysts.

## **■ COMPUTATIONAL RESULTS**

Using first-principles calculations, we examine the hexagonal  $\beta$ -Mo<sub>2</sub>C (011) surface with single-metal dopants that substitutes at all Mo sites, resulting in a one-to-four dopant-to-Mo ratio per layer. We have systematically investigated all different Mo sites up to the seventh subsurface layer. The dopants are selected from the first-row transition and precious metals, namely, Ti, V, Cr, Mn, Fe, Co, Ni, Cu, Zn, Pt, Ir, and Ag. Clearly, the list of the investigated elements is not complete, but here our emphasis is on developing a strategy to explore the materials space rather than performing an exhaustive search over all elements. Note that the (011) termination, which may be referred to as (101) in some literature works, <sup>52</sup> has been identified as the most stable  $\beta$ -Mo<sub>2</sub>C termination. <sup>12,53,54</sup> To assess the segregation tendencies of the dopants, we compute the segregation energy  $\Delta E_{\text{seg}}^{i}$  defined as the energy of a doped surface layer with respect to the energy of a doped "bulk-like" layer.

$$\Delta E_{\text{seg}}^i = E_{M(i)} - E_{M(\text{bulk})} \tag{1}$$

where  $E_{\mathrm{M}(i)}$  and  $E_{\mathrm{M(bulk)}}$  are the energies of the slab with a metal dopant M in the ith and in a "bulklike" layer, respectively. Beyond the seventh surface layer of the slab model,  $E_{\mathrm{M}(i)}$  is found to converge to a constant value, and hence  $E_{\mathrm{M}(i)} \approx E_{\mathrm{M(bulk)}}$ . From eq 1, a negative  $\Delta E_{\mathrm{seg}}^i$  indicates

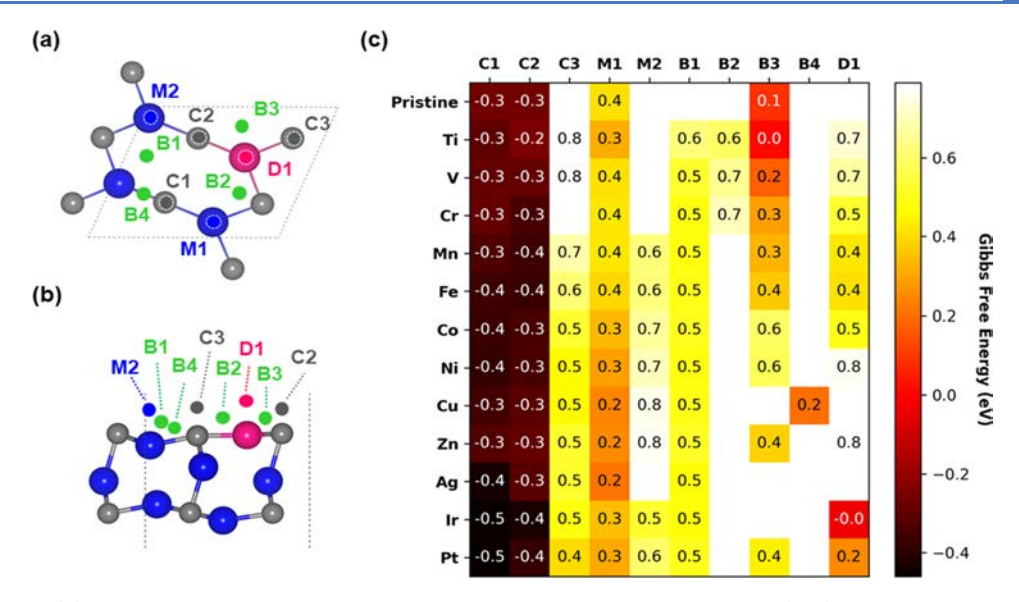


Figure 2. (a) Top and (b) side views for the most stable adsorption sites of the metal-doped β-Mo<sub>2</sub>C (011) surface. Mo atoms are shown as blue, C as gray, H as green, and a metal dopant as pink. Potential hydrogen adsorption sites are shown: C1, C2, and C3 are C top sites; M1 and M2 are Mo top sites; B1, B2, B3, and B4 are bridge sites; and D1 is the top site of a dopant. (c) Hydrogen Gibbs free energy (in eV) at the potential adsorption sites. The whiteouts correspond to unstable adsorption sites.

that a dopant located at the *i*th layer is more thermodynamically stable than at bulk sites.

Figure 1 summarizes  $\Delta E_{\text{seg}}^i$  as a function of the depth of the doping metal site. As seen from the figure,  $\Delta E_{\text{seg}}^1$  values for Pt, Ag, Ir, Cu, Ni, Co, Zn, Fe, and Mn are significantly lower than  $\Delta E_{\text{seg}}^{\prime}$  suggesting that these dopants stabilize at exposed layers rather than at bulk layers. This is notably the case for the precious metals Pt, Ir, and Ag. On the other hand,  $\Delta E_{\rm seg}^{\iota}$ approaches zero for all i's for Cr, Ti, and V dopants, and hence these dopants are likely to spread equally among the different layers. Also, we observe an inverse correlation between the stability of the first-row transition metals and their radii, where smaller-sized dopants are more stable than the larger ones. It is to be noted that the lack of a surface segregation tendency is not cost-effective for precious metal dopants, as only dopants that are on the top surface layers are expected to influence the catalytic activity. In summary, although there are some variations in their segregation tendencies, all dopants can thermodynamically occupy exposed surface sites and thus could potentially influence the HER activity of  $\beta$ -Mo<sub>2</sub>C.

The hydrogen adsorption Gibbs adsorption energy  $\Delta G_{\rm H}$  has been widely accepted <sup>48–50</sup> to accurately predict the experimental measurement of HER rates. For  $\Delta G_{\rm H}=0$ , the HER activity is maximum, while the activity decreases with increasing  $|\Delta G_{\rm H}|$ , in accordance with Sabatier's principle where a reaction has the maximum rate when intermediates interact neither strongly nor weakly with a catalytic surface.  $\Delta G_{\rm H}$  is defined as

$$\Delta G_{\rm H} = \Delta E_{\rm ads} + \Delta E_{\rm ZPE} - T \Delta S \tag{2}$$

where  $\Delta E_{\rm ZPE}$  is the zero-point energy, which is found to be less than 0.05 eV for the doped  $\beta$ -Mo<sub>2</sub>C (011), consistent with prior results for metal surfaces.  $^{48,49,55}$   $\Delta S$  is the change of entropy between hydrogen atoms in the adsorbed state and in the gas state. From experimental measurements,  $\Delta S \sim -\frac{1}{2} S^0_{\rm (H_2)}$ , where  $S^0_{\rm H_2}$ = 1.35 × 10<sup>-3</sup> eV/K is the entropy of hydrogen gas at room temperature.  $^{56}$  The hydrogen adsorption energy  $\Delta E_{\rm ads}$  is defined as

$$\Delta E_{\rm ads} = E_{\rm slab/nH^*} - E_{\rm slab} - \frac{1}{2} E_{\rm H_2}$$
 (3)

where  $E_{\rm slab/H^*}$  and  $E_{\rm slab}$  are the energies of the slab with n adsorbed hydrogen atoms (H\*) and of the clean slab, respectively, and  $E_{\rm H}$ , is the energy of  $H_2$  in the gas phase.

Figure 2 summarizes the hydrogen adsorption sites on pristine and metal-doped  $\beta\text{-Mo}_2\text{C}$  (011) with their corresponding  $\Delta G_{\text{H}}$  probed by a single hydrogen atom. We have verified that  $\Delta G_{\text{H}}$  is nearly independent of hydrogen coverage  $\beta\text{-Mo}_2\text{C}$  (011) due to negligible hydrogen—hydrogen interactions. For the pristine surface, the unique Mo/C composition creates moderate adsorption bridge sites (B3) between two Mo atoms. With the safe assumption that HER largely proceeds through the B3 sites with  $\Delta G_{\text{H}} = \sim 0.1$  eV, the exchange currents are predicted to be  $10^{-5}$  A/cm² using a simple kinetic model, which is consistent with experimental results. The other sites on the pristine surface, namely, the strong adsorption sites with  $\Delta G_{\text{H}} = -0.3$  eV, such as C atop (C1 and C2) sites, and weak adsorption sites with  $\Delta G_{\text{H}} = 0.4$  eV, such as Mo atop (M1) sites, are HER-inactive.

Metal doping creates new adsorption sites on the  $\beta$ -Mo<sub>2</sub>C (011) surface, such as C3, M2, B1, B2, B4, and D1 (see Figure 2a,b). As indicated by large positive  $\Delta G_{\rm H}$  values in Figure 2c, hydrogen adsorption at C3, M2, B1, and B2 sites is endothermic and requires a substantial overpotential in the Volmer step. Doping, however, introduces thermoneutral sites—B3 on the Ti-doped surface and D1 on the Ir-doped surface—that are expected to be more HER-active than on pristine  $\beta$ -Mo<sub>2</sub>C (011), as the sites are characterized by  $\Delta G_{\rm H}$  = -0.01 and -0.04 eV, respectively. The concentrations of the active sites on pristine, Ir-doped, and Ti-doped  $\beta$ -Mo<sub>2</sub>C (011) are identical, assuming that only sites with  $|\Delta G_H| < 0.1$  eV are active for HER. Compared to the pristine surface, Ir and Ti dopants significantly improve the HER activities by introducing new HER-active sites, while the other dopants annihilate the original active sites of the  $\beta$ -Mo<sub>2</sub>C (011) surface. Given that (011) is a stable termination, representing the  $\beta$ -Mo<sub>2</sub>C catalyst under electrochemical and synthesis conditions, and

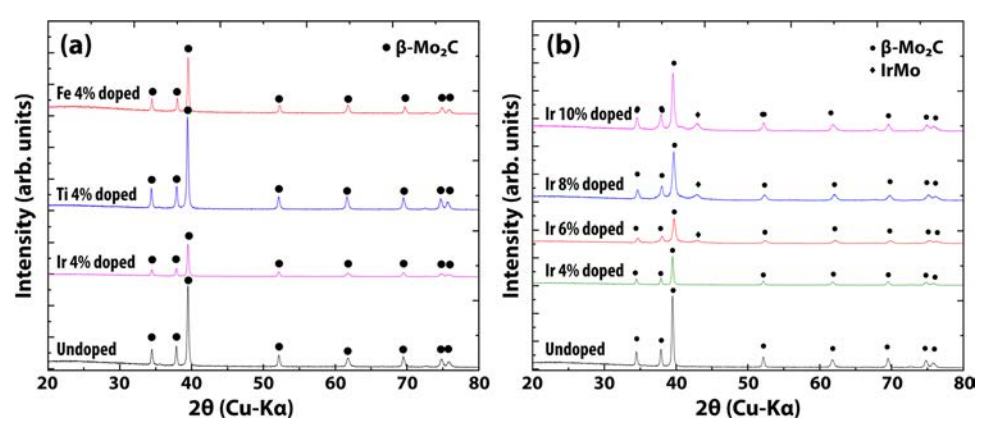


Figure 3. (a) XRD patterns of pristine and 4% Ir/Ti/Fe-doped Mo<sub>2</sub>C NPs supported on 3 wt % graphene oxide mixture films. (b) XRD patterns of pristine and (4, 6, 8, 10%) Ir-doped  $\beta$ -Mo<sub>2</sub>C NPs supported on 3 wt % graphene oxide mixture films.

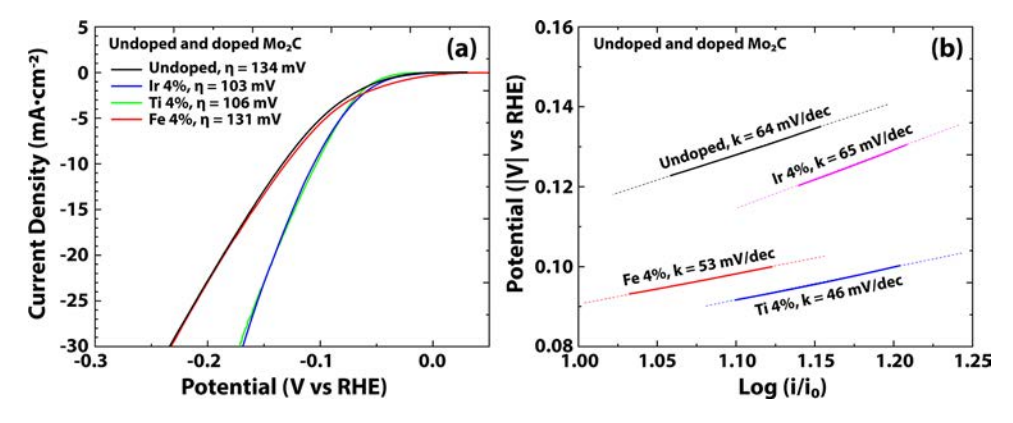


Figure 4. (a) HER polarization curves and (b) Tafel plots for pristine and Ir-, Ti-, and Fe-doped β-Mo<sub>2</sub>C.

only the sites corresponding to  $\Delta G_{\rm H} \approx 0$  contribute the most to HER among the other sites, we expect that Ir and Ti doping can significantly improve HER activity.

#### EXPERIMENTAL RESULTS

To validate the computational predictions, we use a microwave-assisted solvothermal method to synthesize pristine, Irdoped, Ti-doped, and Fe-doped  $\beta$ -Mo<sub>2</sub>C NPs supported on graphene oxide nanosheets. Note that we will focus first on comparing experimental results for pristine, Ir-doped, and Tidoped  $\beta$ -Mo<sub>2</sub>C. Figure 3a shows the XRD patterns of pristine  $\beta$ -Mo<sub>2</sub>C NPs and the NPs doped with 4% Ir and Ti. The pristine  $\beta$ -Mo<sub>2</sub>C NPs exhibit sharp diffraction peaks that are indexed as hexagonal  $\beta$ -Mo<sub>2</sub>C (JCPDS pattern: 35-05-0787). No second phase is found in the XRD pattern of pristine  $\beta$ - $Mo_2C$  NPs. When the pristine  $\beta$ - $Mo_2C$  NPs are doped with 4% Ir and Ti, we observe no crystal structure change other than a small decrease in lattice parameters. In Figure 3b, we show the XRD patterns of the pristine  $\beta$ -Mo<sub>2</sub>C NPs doped with different percentages of Ir dopants. When more than 4% of Ir is doped, the formation of an Ir-Mo phase is indicated by the broad diffraction peak at  $2\theta = 43^{\circ}$ . In none of the patterns is an amorphous or noncrystalline Mo<sub>v</sub>C phase detected in any meaningful quantity. As the Ir-Mo phase exhibits different HER behaviors from the Ir-doped phase (see Figure S2a,b), we limited the doping concentration to 4% for all dopants for subsequent electrochemical analysis of HER activity.

Linear sweep voltammetry is performed at a 20 mV s<sup>-1</sup> scan rate in 0.5 M  $H_2SO_4$  electrolyte on pristine, 4% Ir-doped, and 4% Ti-doped  $\beta$ -Mo<sub>2</sub>C NPs. The cyclic voltammograms of the

samples are shown in Figure 4a. To compare relative HER activities, the overpotential values  $\eta_{10}$  determined at a current density of 10 mA/cm² are 134, 106, and 103 mV for the pristine, 4% Ir-doped, and 4% Ti-doped  $\beta$ -Mo<sub>2</sub>C NPs, respectively. With Ir or Ti doping,  $\eta_{10}$  is reduced by ~20% compared to the pristine  $\beta$ -Mo<sub>2</sub>C NPs. Figure 4b shows the Tafel plots deduced from Figure 4a. For pristine, 4% Ir-doped, and 4% Ti-doped  $\beta$ -Mo<sub>2</sub>C NPs, the Tafel slopes are 64, 53, and 46 mV/dec, respectively. The corresponding exchange current densities are  $5.37 \times 10^{-5}$ ,  $1.78 \times 10^{-4}$ , and  $2.24 \times 10^{-4}$  A/cm², as obtained based on Tafel slopes.

Electrochemically active surface area (ECSA) analysis is performed using cyclic voltammetry. Figure 5 shows the changes in the current densities as a function of the scan rate. The double-layer capacitance ( $C_{\rm dl}$ ) is measured at scan rates from 5 to 200 mV/s, with an increment of 16 mV/s, in nonfaradic potentials from 0.1 to 0.3 V vs RHE. The  $C_{\rm dl}$  of pristine  $\beta$ -Mo<sub>2</sub>C is 12 mF/cm<sup>2</sup>, as determined in our recent study. In contrast, 4% Ir and 4% Ti doping increases the  $C_{\rm dl}$  to 18.3 and 22.8 mF/cm<sup>2</sup>, respectively, almost doubling that of the pristine  $\beta$ -Mo<sub>2</sub>C NPs. According to our computational predictions, the concentrations of active sites on the pristine and metal-doped Mo<sub>2</sub>C  $\beta$ -(011) are the same, which indicates that Ti and Ir dopants have a dramatic effect on the chemistry of electrochemical active sites of  $\beta$ -Mo<sub>2</sub>C.

The experimentally measured electrochemical performances for Ir and Ti show HER enhancements based on lower overpotentials and higher exchange currents than pristine  $\beta$ -Mo<sub>2</sub>C, which agrees with theoretical predictions that Ir doping creates new active sites, i.e., D1 sites, and Ti doping alters the

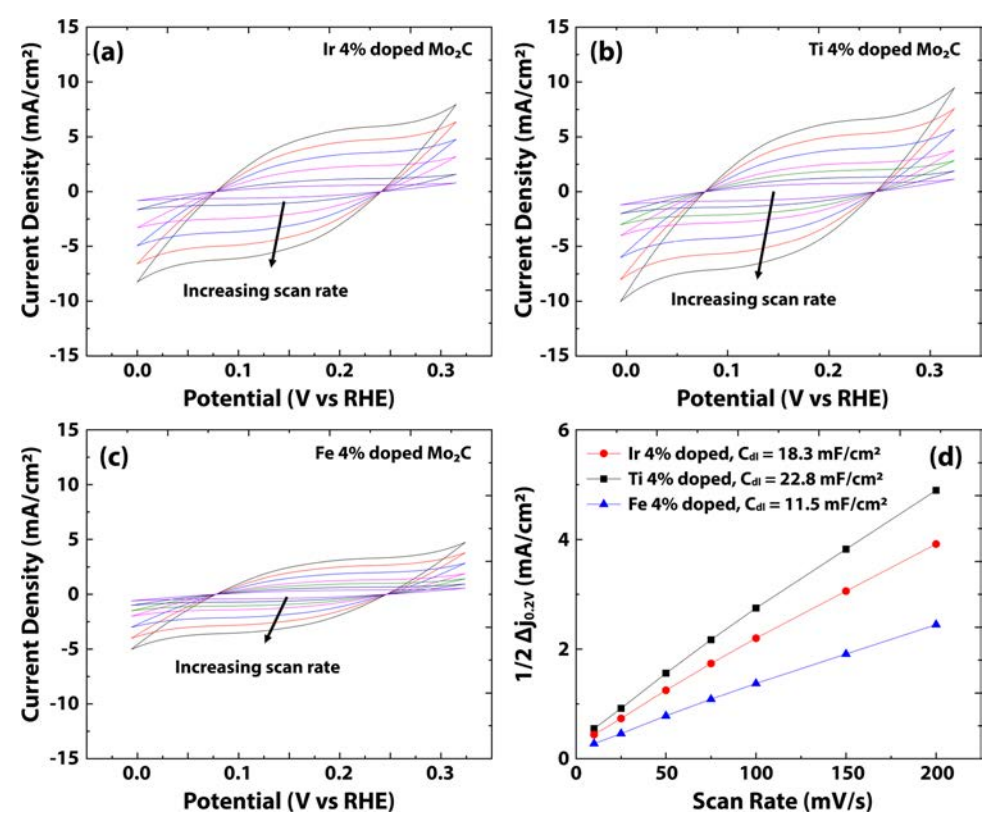
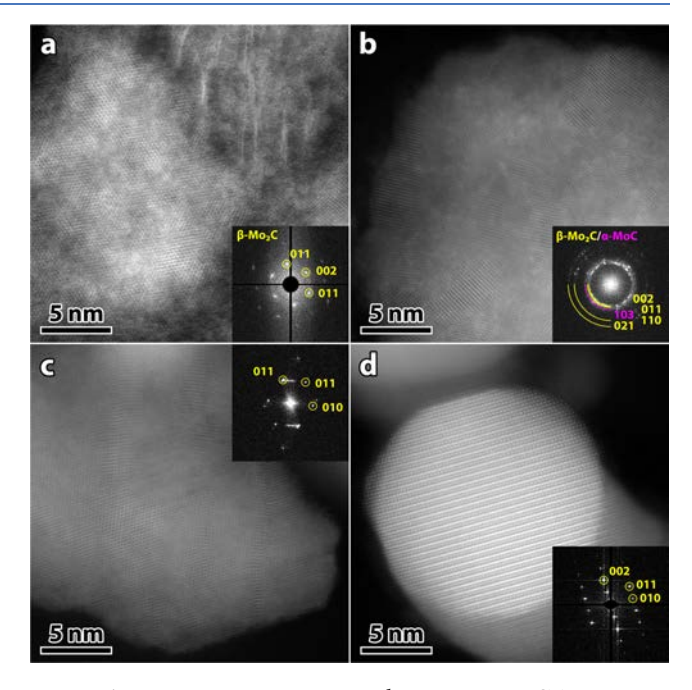


Figure 5. Current density—potential curves of (a) Ir 4%-doped, (b) Ti 4%-doped, (c) Fe 4%-doped Mo<sub>2</sub>C-3 wt % graphene oxide (GO) mixture films, cycled between 0.0 and 0.3 V (vs RHE) at a scan rate from 5 to 200 mV s<sup>-1</sup> in an acidic medium, and (d)  $0.5\Delta J_{0.2V}$  (half of the current density difference at 0.2 V) as a function of the scan rate.

active sites on pristine  $\beta$ -Mo<sub>2</sub>C to be thermoneutral. However, based only on electrochemical measurements, it is premature to argue for agreement, or lack thereof, between theory and the experiment. Namely, it is important to ensure that the theoretical models in terms of the Mo<sub>2</sub>C phase, metal dispersion, and surface termination are consistent with the synthesized samples.

Fully interpreting the electrochemical data requires knowledge of the nanoscale structure and chemistry from which it arises, in particular, particle size and morphology, and the presence of dopant dispersion or segregation. To obtain this information, we employed transmission electron microscopy (TEM), high-angle annular dark-field scanning TEM (HAADF-STEM), and energy-dispersive X-ray spectroscopy (EDS). In general, the pristine and metal-doped  $\beta$ -Mo<sub>2</sub>C NPs are fused together either directly or with a carbonaceous material in-between, possessing morphologies ranging from nearly spherical to faceted and isotropic to high aspect ratio, as shown in Figure S3. Atomic-resolution HAADF-STEM and HRTEM images of the NPs are shown in Figures 6 and S3, respectively. Selected area electron diffraction (SAED) (Figure S3) and fast Fourier transform (FFT) analyses reveal that the NPs are predominantly in the  $\beta$ -Mo<sub>2</sub>C phase, but varying amounts of NPs in the  $\alpha$ -MoC phase are observed, especially for 4% Ir-doped NPs. For simplicity, and due to the significantly smaller presence of  $\alpha$ -MoC, only  $\beta$ -Mo<sub>2</sub>C is mentioned in subsequent references to Mo<sub>v</sub>C with the existence of additional phases in this work. Most of the NPs are not sharply faceted, but in those NPs with a high degree of faceting, such as in Figure S4a,d, the (011), (002), and (100) facets predominated, with the former being slightly more



**Figure 6.** Representative atomic-resolution HAADF-STEM micrographs of (a) pristine  $\beta$ -Mo<sub>2</sub>C, (b) 4% Ir-doped, (c) 8% Ti-doped, and (d) 7.5% Fe-doped samples. Insets show the corresponding FFT patterns for each image, indexed to (yellow)  $\beta$ -Mo<sub>2</sub>C and (magenta) α-MoC. (Note: some plane spacings have many potential corresponding planes. Here, one plane has been chosen to represent each given spacing).

common. Additional morphological and structural details are included in the Supporting Information.

No evidence of dopant segregation is observed from the contrast in HAADF-STEM images of the Fe- and Ti-doped specimens (e.g., Figure 6d,c). In the 4% Ir-doped specimen (Figure 6b), copious amounts of few-atom nanoclusters are observed uniformly distributed all over the  $\beta$ -Mo<sub>2</sub>C particles, either decorating the surface or incorporated into the surface layer(s). The increased image intensity of these nanoclusters compared to that of the Mo<sub>2</sub>C support indicates they are Ir, as the image intensity is predominantly atomic-mass-dependent under the imaging conditions used. Occasional small Ir-rich NPs are also observed on the surface, but they are uncommon in comparison.

The size distributions of the pristine and metal-doped  $\beta$ -Mo<sub>2</sub>C NPs are plotted in Figure 7. Population summary

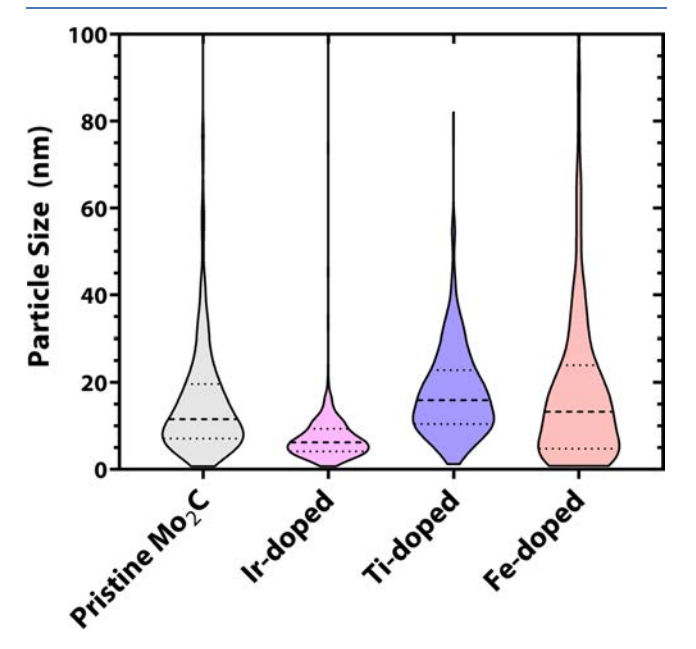


**Figure 7.** Violin plots (kernel density estimates) of β-Mo<sub>2</sub>C NP sizes. Dashed lines indicate the median, and dotted lines indicate the quartiles. The vertical axis has been truncated for easier comparison of the distributions. Nominal metal doping for Ir, Ti, and Fe is 8, 8, and 7.5%, respectively. Swarm plot versions of these distributions are included in Figure S5. Colors correspond to those used in Figure 3a for identifying the dopants.

statistics and the calculation details are described in Table ST1. The average size of pristine  $\beta$ -Mo<sub>2</sub>C NPs (15.8  $\pm$  15.0 nm) is slightly smaller than the size of Ti-doped NPs (17.8  $\pm$  10.6 nm). In contrast, the size of Ir-doped NPs is significantly narrower and of a smaller mean (8.9  $\pm$  22.6 nm, with a 75% percentile of 9.3 nm) than any other sample. The Ir-doped  $\beta$ -Mo<sub>2</sub>C NPs possessed large quantities of small (<10 nm) particles, whereas relatively few are observed in the Ti-doped NPs.

EDS elemental mapping is employed to verify and quantify NP composition and dopant dispersion. Example maps are provided in Figure 8a-c—at higher magnification to observe intraparticle distribution—and Figure 8d-f—at lower magnification to examine distribution at the aggregate level. The sum spectra for these maps are shown in Figures S7 and S8, respectively, and quantification of the ratio of dopant metals to Mo is listed in Table ST2. Ti-doped samples exhibit uniform

incorporation of dopants, with no segregation observed. The surface segregation of the Ir dopant and the appearance of occasional Ir-rich NPs suggest that 4 atom % is at the limit of Ir incorporation in  $\beta$ -Mo<sub>2</sub>C prepared via these methods. Above 4 atom %, Ir-rich NPs nucleated on  $\beta$ -Mo<sub>2</sub>C, which have additional HER-active sites other than our focus on Ir-doped  $\beta$ -Mo<sub>2</sub>C. Although the Ti- and Fe-doped samples examined in TEM are of higher dopant concentrations than those tested electrochemically, the lack of any observed segregation even at these higher dopant levels indicates that segregation is highly unlikely to occur at lower concentrations. This is in contrast to the Ir-doped sample, where segregation is observed at 8%, and thus the lower concentration warranted examination. More information on the Ir-doped  $\beta$ -Mo<sub>2</sub>C morphology characterization with different atom % values is included in the SI.

#### DISCUSSION

The experimental results are in accordance with computational analysis. From cyclic voltammetry, we find that the exchange current densities for Ir- and Ti-doped  $\beta$ -Mo<sub>2</sub>C NPs are 1.78  $\times$  $10^{-4}$  and  $2.24 \times 10^{-4}$  A/cm<sup>2</sup>, respectively, which are nearly one order of magnitude higher than that of pristine  $\beta$ -Mo<sub>2</sub>C NPs with  $5.37 \times 10^{-5}$  A/cm<sup>2</sup>. In addition, the overpotential for the pristine  $\beta$ -Mo<sub>2</sub>C NPs is ~20% less than those for the Irand Ti-doped  $\beta$ -Mo<sub>2</sub>C NPs. This agrees with the computational findings that Ir- and Ti-doped  $\beta$ -Mo<sub>2</sub>C (011) samples have nearly thermoneutral sites with  $\Delta G_{\rm H} \approx 0$  that are more HER-active than the sites on pristine  $\beta$ -Mo<sub>2</sub>C (011) with  $\Delta G_{\rm H}$  $\approx$  0.1 eV. We posit that the enhanced HER on Ir- and Tidoped  $\beta$ -Mo<sub>2</sub>C is due to the new active sites facilitated by the dopants based on the following reasons: (1) the Tafel slopes of the Ir-doped and Ti-doped  $\beta$ -Mo<sub>2</sub>C NPs are different from the Tafel slope of the pristine  $\beta$ -Mo<sub>2</sub>C NPs. This supports our modeling results that there are new active sites for HER that are generated by doping. (2) XRD, STEM, and EDS confirm that doping with Ir and Ti does not cause a phase change of  $\beta$ - $Mo_2C$ ; only a negligible amount of the  $\alpha$ -MoC phase appears in Ir-doped  $\beta$ -Mo<sub>2</sub>C NPs. This agrees with our computational results showing that the Ir dopants homogeneously segregate into the upper layers of the  $\beta$ -Mo<sub>2</sub>C NPs, while the Ti dopants are equally distributed among all layers. As we do not detect any of the amorphous or noncrystalline phases of the metaldoped  $\beta$ -Mo<sub>2</sub>C, and we have ruled out the effects of Ir segregation, these findings suggest that the HER activities mainly come from the metal-doped  $\beta$ -Mo<sub>2</sub>C (011) terminations. (3) From ECSA, the values of  $C_{\rm dl}$  for Ir- and Ti-doped  $\beta$ -Mo<sub>2</sub>C NPs nearly double the value for pristine  $\beta$ -Mo<sub>2</sub>C NPs. The larger ECSA on the doped  $\beta$ -Mo<sub>2</sub>C NPs suggests higher HER activities than the pristine  $\beta$ -Mo<sub>2</sub>C NPs, assuming that the surface areas of the samples are similar.

To further enhance our rationalization of the connections between the computational and experimental results, we also examined Fe-doped  $\beta$ -Mo<sub>2</sub>C NPs, which are predicted to be nonoptimal for HER based on our first-principles calculations (see Figure 2c). Fe doping is selected because previous studies are controversial, reporting both insignificant<sup>45</sup> and significant<sup>45,46</sup> improvements for the HER activity of Fe-doped  $\beta$ -Mo<sub>2</sub>C. From the electrochemical analysis, we find for the Fe-doped NPs that the overpotential 131 mV, exchange current 4.79  $\times$  10<sup>-5</sup> A/cm<sup>2</sup>, and  $C_{\rm dl}$  11.5 mF/cm<sup>2</sup> are of similar magnitude to the corresponding values for pristine  $\beta$ -Mo<sub>2</sub>C NPs. We posit that the HER activity on Fe-doped  $\beta$ -Mo<sub>2</sub>C NPs arises from the active sites of pristine  $\beta$ -Mo<sub>2</sub>C NPs based

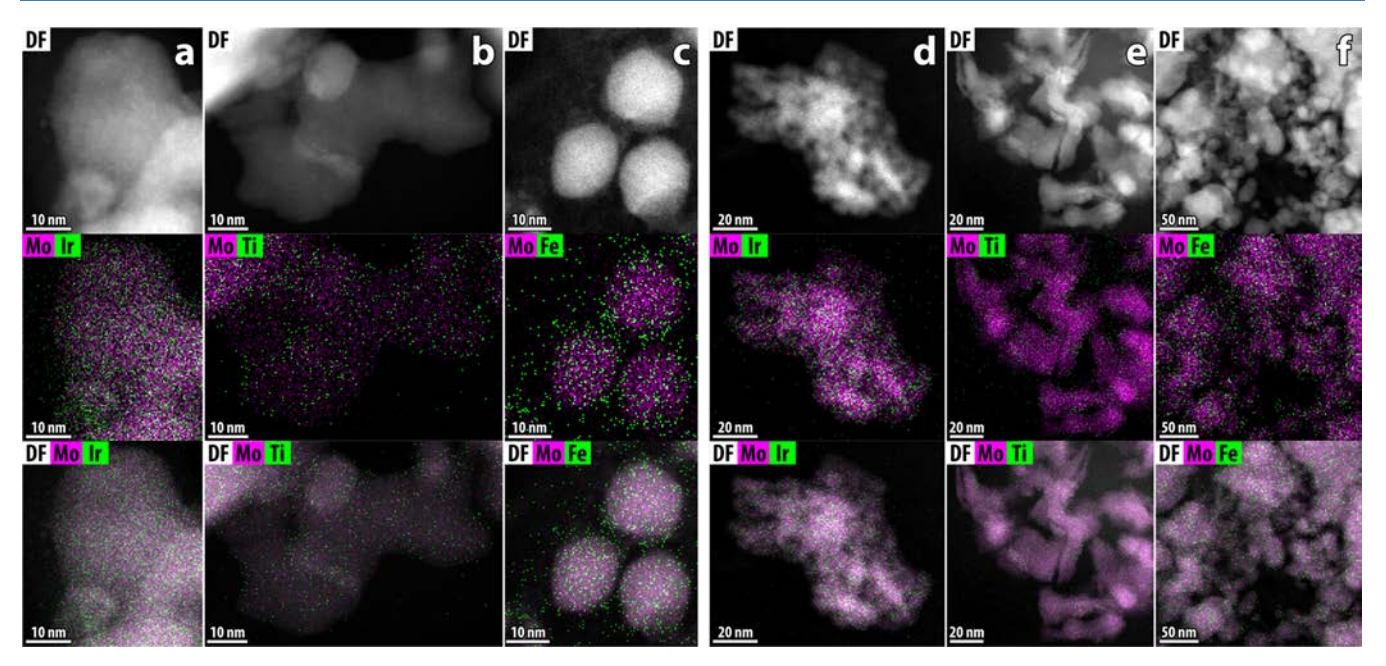


Figure 8. Background-subtracted EDS elemental maps from β-Mo<sub>2</sub>C NPs doped with (a, d) 4% Ir, (b, e) 8% Ti, and (c, f) 7.5% Fe. The middle images are Mo (magenta) + primary metal (Ir, Ti, Fe; green) maps, while the bottom images have been overlain onto the HAADF image. Elemental quantification is provided in Table ST2.

on the following findings: (1) Our computations show that the sites on pristine  $\beta$ -Mo<sub>2</sub>C (011) with  $\Delta G_{\rm H}=0.1$  eV are significantly more active than the new sites on Fe-doped  $\beta$ -Mo<sub>2</sub>C (011) that are either too strong,  $\Delta G_{\rm H}=-0.4$ , or too weak,  $\Delta G_{\rm H}>0.4$  eV; and (2) the experiments find that Fe doping generates NPs of smaller size. Although the mean size of  $\beta$ -Mo<sub>2</sub>C NPs somewhat increases with Fe doping compared to that of pristine, 15.8  $\pm$  15.0 and 20.4  $\pm$  24.7 nm, respectively, it substantially increases the relative number of small particles (<5 nm, see Figure S5). This suggests that the HER current for Fe-doped  $\beta$ -Mo<sub>2</sub>C NPs is expected to be slightly higher than that of the pristine  $\beta$ -Mo<sub>2</sub>C NPs as the active sites on pristine  $\beta$ -Mo<sub>2</sub>C NPs are more exposed on smaller particles than on larger ones.

#### CONCLUSIONS

We computationally screen 12 metal dopants from first-row transition metals (Ti, V, Cr, Mn, Fe, Co, Ni, Cu, Zn) and precious metals (Pt, Ir, Ag) on  $\beta$ -Mo<sub>2</sub>C with respect to HER activity enhancement. We find that only Ir and Ti doping introduces new HER-active sites that bind hydrogen thermoneutrally and thus are expected to enhance the catalytic activity. For validation, we synthesize metal-doped  $\beta$ -Mo<sub>2</sub>C NPs using a microwave-assisted solvothermal method. Cyclic voltammetry measurements show that the overpotential decreases by  $\sim 20\%$  when pristine  $\beta$ -Mo<sub>2</sub>C NPs are doped with Ir or Ti. Also, the exchange currents for Ir- and Ti-doped  $\beta$ -Mo<sub>2</sub>C are, respectively, 1.78 × 10<sup>-4</sup> and 2.24 × 10<sup>-4</sup> A/cm<sup>2</sup>, which are nearly one order of magnitude larger than the corresponding value of  $5.37 \times 10^{-5}$  A/cm<sup>2</sup> for the pristine  $\beta$ -Mo<sub>2</sub>C NPs. Fe doping is found not to enhance the HER currents based on computational and electrochemical experimental results. Further, we employ TEM, HAADF-STEM, and EDS to examine the atomic structure of the metal-doped  $\beta$ -Mo<sub>2</sub>C. We find that Ir and Fe are favorable to segregating on the exposed surface and Ti tends to distribute equally among the layers, which agrees with our computational analysis of segregation tendencies. From showing that there is a larger proportion of small NPs in Fe-doped  $\beta$ -Mo<sub>2</sub>C NPs than that in the Ir- and Ti-doped  $\beta$ -Mo<sub>2</sub>C NPs, we justify that the HER is activated by Ir and Ti dopants rather than by exposing original sites due to the increase of effective surface area. We have confirmed that Ir and Ti doping enhances HER activity by manipulating the catalytic chemistry, which demonstrates the synergetic role of computational and experimental approaches in rationalizing the design of enhanced catalysts.

## METHODS

First-Principles Calculations. Density functional theory (DFT) calculations with the Revised-Perdew-Burke-Ehrenzhof (revPBE) exchange-correlation functional are carried out to determine the stability and HER reactivity of doped  $\beta$ -Mo<sub>2</sub>C surfaces. The surface models are cleaved from the bulk  $\beta$ -Mo<sub>2</sub>C with a hexagonal structure. <sup>58</sup> We focus on mixed Mo/C (011) as it is the most stable termination among low-Millerindex surfaces of  $\beta$ -Mo<sub>2</sub>C under common synthesis conditions. 12,53,54 Further, such a surface shows enhanced activity toward HER. Note that the (011) surface is referred to as the (101) surface in some studies. 12,53 We use a supercell approach to represent the slab models with 14 layers cleaved from (1  $\times$ 1) supercells with the same atomic structure in the top and the bottom layers. All of the atoms in the slab models are relaxed to assess their stability. Atoms that are more than three layers below the exposed layer showed very little relaxations compared to the pristine bulk positions, suggesting that the slab models have negligible finite-size dependence.

Pristine and Metal-Doped β-Mo<sub>2</sub>C Synthesis. β-Mo<sub>2</sub>C nanoparticles (NPs) are synthesized by the microwave-assisted solvothermal method using MoCl<sub>5</sub> (99.6%, Alfa Aesar), ethanol (200 proof, Decon), urea (Sigma-Aldrich), TiCl<sub>4</sub> (0.09M in 20% HCl, Sigma-Aldrich), IrCl<sub>3</sub>·3H<sub>2</sub>O (53–56% Ir, Acros Organics), FeCl<sub>3</sub>·6H<sub>2</sub>O (97%, Sigma-Aldrich) and graphene oxide nanosheets (ACS Material). Doping is achieved by mixing 1 g of MoCl<sub>5</sub> and the dopant in 5 ml of

ethanol for 10 min, followed by the addition of urea (7 molar ratio). After vigorous mixing, 3 wt% graphene oxide (GO) nanosheets (1–5  $\mu \rm m$  in diameter) in comparison to the weight of  $\beta \rm -Mo_2 C$  NP is added to the precursor solution. The fully mixed solution is reacted with microwave radiation (CEM microwave reactor) until the solution temperature reaches 150 °C and is then held at this temperature for 10 min. Microwave power and pressure are maintained at 800 W and 800 kpsi, respectively, throughout the reaction. After the reaction, the amorphous solid is collected and subsequently crystallized at 800 °C for 180 min under a  $\rm N_2$  atmosphere.

**TEM Characterization.** Specimens for TEM examination are prepared via drop casting, wherein small quantities of the powdered sample are dispersed in ethanol and sonicated for 1 min to uniformly disperse the particles in solution. A 4  $\mu$ L droplet of each solution is then pipetted onto ultrathin carboncoated Cu TEM grids (Ted Pella Inc.) and allowed to dry. These specimens are subsequently examined using a Thermo Fisher Themis G2 200 probe-aberration-corrected S/TEM operating at 200 kV and equipped with a Super-X energydispersive X-ray spectroscopy system for elemental mapping and quantification (using Velox software). A probe current of 45 pA is used for high-angle annular dark-field (HAADF) STEM imaging, and a 300-425 pA probe current is used for EDS mapping. The Circular Hough Transform plugin<sup>59</sup> for Gatan Digital Micrograph is used to measure diffraction ring spacing in any ring pattern, and a custom-scripted worksheet is employed to match diffraction and FFT spacings against a library of plane spacings.

Electrochemistry and XRD. The crystal structure, size, morphology, and composition of the synthesized materials are determined using X-ray diffraction (XRD), scanning electron microscopy (SEM), and scanning transmission electron microscopy (STEM). XRD (X'Pert PaNalytical) patterns of the samples are measured. For HER testing, 1 g of undoped or doped Mo<sub>2</sub>C NPs is mixed with 0.08 g of ethyl cellulose and 4.46 g of  $\alpha$ -terpinol. Each mixture is then processed with a three-roll mill (Model 50i, Exakt) to form a paste. The paste is coated onto fluorine-doped tin oxide (FTO) glass using a screen-printing process, and the organic part of the paste is slowly burned away at 250 °C for 3 h in a tubular furnace under a N2 atmosphere. The geometrical surface area of the electrode is 1 cm<sup>2</sup> and the catalyst loading is 0.54 mg/cm<sup>2</sup> for all β-Mo<sub>2</sub>C NPs or Mo<sub>2</sub>C-GO electrodes. The electronic properties of the printed thick films are determined using fourpoint probe electric conductivity measurements. All electrochemical measurements are performed using a three-electrode electrochemical workstation (CHI 660 potentiostat). A saturated calomel electrode (SCE) and Pt plate are chosen as the reference and counter electrodes, respectively, and are deaerated with argon before use. The  $\beta$ -Mo<sub>2</sub>C electrode is tested in a 0.5 M H<sub>2</sub>SO<sub>4</sub> aqueous electrolyte. Polarization curves are obtained through linear sweep voltammetry (LSV) in 0.5 M H<sub>2</sub>SO<sub>4</sub> at a scan rate of 20 mV/s.

## ASSOCIATED CONTENT

#### Supporting Information

The Supporting Information is available free of charge at https://pubs.acs.org/doi/10.1021/acscatal.2c03184.

Computational details, atomic structure of surfaces, HER polarization curves, TEM micrographs, Mo<sub>2</sub>C

particle morphology and structure, STEM-EDS, and pseudopotential information (PDF)

## AUTHOR INFORMATION

## **Corresponding Authors**

Jung-Kun Lee – Department of Materials Science and Engineering, University of Pittsburgh, Pittsburgh, Pennsylvania 15260, United States; ⊚ orcid.org/0000-0002-7778-7679; Email: jul37@pitt.edu

Wissam A. Saidi – Department of Materials Science and Engineering, University of Pittsburgh, Pittsburgh, Pennsylvania 15260, United States; oocid.org/0000-0001-6714-4832; Email: alsaidi@pitt.edu

#### **Authors**

Timothy T. Yang — Department of Materials Science and Engineering, University of Pittsburgh, Pittsburgh, Pennsylvania 15260, United States; orcid.org/0000-0002-5785-0511

Anqi Wang — Department of Materials Science and Engineering, University of Pittsburgh, Pittsburgh, Pennsylvania 15260, United States

Stephen D. House — Department of Chemical and Petroleum Engineering and Environmental TEM Catalysis Consortium (ECC), University of Pittsburgh, Pittsburgh, Pennsylvania 15260, United States; orcid.org/0000-0003-2035-6373

Judith Yang – Department of Chemical and Petroleum Engineering, Environmental TEM Catalysis Consortium (ECC), and Department of Physics and Astronomy, University of Pittsburgh, Pittsburgh, Pennsylvania 15260, United States

Complete contact information is available at: https://pubs.acs.org/10.1021/acscatal.2c03184

#### Notes

The authors declare no competing financial interest.

#### ACKNOWLEDGMENTS

The authors acknowledge financial support from the National Science Foundation (Award No. CBET-2130804). The authors are grateful for computing time provided in part by the CRC resources at the University of Pittsburgh and Argonne Leadership Computing Facility, which is a DOE Office of Science User Facility supported under Contract DE-AC02-06CH11357. Electron microscopy is performed at the Nanoscale Fabrication and Characterization Facility at the University of Pittsburgh. This research used resources of the Environmental TEM Catalysis Consortium (ECC), which is supported by the University of Pittsburgh and Hitachi High Technologies.

#### REFERENCES

- (1) Dresselhaus, M. S.; Thomas, I. L. Alternative energy technologies. *Nature* **2001**, 414, 332.
- (2) Rivard, E.; Trudeau, M.; Zaghib, K. Hydrogen Storage for Mobility: A Review. *Materials* **2019**, *12*, No. 1973.
- (3) Griffiths, S.; Sovacool, B. K.; Kim, J.; Bazilian, M.; Uratani, J. M. Industrial decarbonization via hydrogen: A critical and systematic review of developments, socio-technical systems and policy options. *Energy Research & Social Science* **2021**, *80*, No. 102208.
- (4) National Academies of Sciences, E. & Medicine Advances, Challenges, and Long-Term Opportunities in Electrochemistry: Addressing

- Societal Needs: Proceedings of a Workshop—in Brief, The National Academies Press, 2020.
- (5) Humagain, G.; MacDougal, K.; MacInnis, J.; et al. Highly Efficient, Biochar-Derived Molybdenum Carbide Hydrogen Evolution Electrocatalyst. *Adv. Energy Mater.* **2018**, *8*, No. 1801461.
- (6) Huang, Y.; Ge, J.; Hu, J.; et al. Nitrogen-Doped Porous Molybdenum Carbide and Phosphide Hybrids on a Carbon Matrix as Highly Effective Electrocatalysts for the Hydrogen Evolution Reaction. *Adv. Energy Mater.* **2018**, *8*, No. 1701601.
- (7) Wan, C.; Regmi, Y. N.; Leonard, B. M. Multiple phases of molybdenum carbide as electrocatalysts for the hydrogen evolution reaction. *Angew. Chem., Int. Ed.* **2014**, *53*, 6407–6410.
- (8) Politi, J. R. d. S.; Viñes, F.; Rodriguez, J. A.; Illas, F. Atomic and electronic structure of molybdenum carbide phases: bulk and low Miller-index surfaces. *Phys. Chem. Chem. Phys.* **2013**, *15*, 12617–12625.
- (9) Hugosson, H. W.; et al. Theory of phase stabilities and bonding mechanisms in stoichiometric and substoichiometric molybdenum carbide. *AIP J. Appl. Phys.* **1999**, *86*, 3758–3767.
- (10) Baek, D. S.; Lee, J.; Kim, J.; Joo, S. H. Metastable Phase-Controlled Synthesis of Mesoporous Molybdenum Carbides for Efficient Alkaline Hydrogen Evolution. *ACS Catal.* **2022**, *12*, 7415–7426.
- (11) Tang, C.; Zhang, H.; Xu, K.; et al. Unconventional molybdenum carbide phases with high electrocatalytic activity for hydrogen evolution reaction. *J. Mater. Chem. A* **2019**, *7*, 18030–18038.
- (12) Yang, T. T.; Saidi, W. A. Tuning the hydrogen evolution activity of  $\beta$ -Mo2C nanoparticles via control of their growth conditions. *Nanoscale* **2017**, *9*, 3252–3260.
- (13) Wu, H. B.; Xia, B. Y.; Yu, L.; Yu, X.-Y.; Lou, X. W. Porous molybdenum carbide nano-octahedrons synthesized via confined carburization in metal-organic frameworks for efficient hydrogen production. *Nat. Commun.* **2015**, *6*, No. 6512.
- (14) Chen, W. F.; Wang, C. H.; Sasaki, K.; et al. Highly active and durable nanostructured molybdenum carbide electrocatalysts for hydrogen production. *Energy Environ. Sci.* **2013**, *6*, No. 943.
- (15) Šljukić, B.; Santos, D. M. F.; Vujković, M.; et al. Molybdenum Carbide Nanoparticles on Carbon Nanotubes and Carbon Xerogel: Low-Cost Cathodes for Hydrogen Production by Alkaline Water Electrolysis. *ChemSusChem* **2016**, *9*, 1200–1208.
- (16) Youn, D. H.; Han, S.; Kim, J. Y.; et al. Highly Active and Stable Hydrogen Evolution Electrocatalysts Based on Molybdenum Compounds on Carbon Nanotube—Graphene Hybrid Support. *ACS Nano* **2014**, *8*, 5164—5173.
- (17) Li, J. S.; Wang, Y.; Liu, C. H.; et al. Coupled molybdenum carbide and reduced graphene oxide electrocatalysts for efficient hydrogen evolution. *Nat. Commun.* **2016**, *7*, No. 11204.
- (18) Wang, B.; Wang, G.; Wang, H. Hybrids of Mo2C nanoparticles anchored on graphene sheets as anode materials for high performance lithium-ion batteries. *J. Mater. Chem. A* **2015**, *3*, 17403–17411.
- (19) He, C.; Tao, J. Exploration of the electrochemical mechanism of ultrasmall multiple phases molybdenum carbides nanocrystals for hydrogen evolution reaction. *RSC Adv.* **2016**, *6*, 9240–9246.
- (20) He, C.; Tao, J. Synthesis of nanostructured clean surface molybdenum carbides on graphene sheets as efficient and stable hydrogen evolution reaction catalysts. *Chem. Commun.* **2015**, *51*, 8323–8325.
- (21) Pan, L. F.; Li, Y. H.; Yang, S.; et al. Molybdenum carbide stabilized on graphene with high electrocatalytic activity for hydrogen evolution reaction. *Chem. Commun.* **2014**, *50*, 13135–13137.
- (22) Liu, X.; Deng, Y.; Zheng, L.; et al. Engineering Low-Coordination Single-Atom Cobalt on Graphitic Carbon Nitride Catalyst for Hydrogen Evolution. ACS Catal. 2022, 12, 5517–5526.
- (23) Reynard, D.; Nagar, B.; Girault, H. Photonic Flash Synthesis of Mo2C/Graphene Electrocatalyst for the Hydrogen Evolution Reaction. ACS Catal. 2021, 11, 5865–5872.
- (24) Ojha, K.; Saha, S.; Kolev, H.; Kumar, B.; Ganguli, A. K. Composites of graphene-Mo 2 C rods: highly active and stable

- electrocatalyst for hydrogen evolution reaction. *Electrochim. Acta* **2016**, 193, 268–274.
- (25) Zhang, K.; Zhao, Y.; Fu, D.; Chen, Y. Molybdenum carbide nanocrystal embedded N-doped carbon nanotubes as electrocatalysts for hydrogen generation. *J. Mater. Chem. A* **2015**, *3*, 5783–5788.
- (26) Lu, C.; Tranca, D.; Zhang, J.; et al. Molybdenum Carbide-Embedded Nitrogen-Doped Porous Carbon Nanosheets as Electrocatalysts for Water Splitting in Alkaline Media. *ACS Nano* **2017**, *11*, 3933–3942.
- (27) Cheng, Y.; Gong, J.; Cao, B.; et al. An Ingenious Strategy to Integrate Multiple Electrocatalytically Active Components within a Well-Aligned Nitrogen-Doped Carbon Nanotube Array Electrode for Electrocatalysis. *ACS Catal.* **2021**, *11*, 3958–3974.
- (28) Tang, Y.; Yang, C.; Sheng, M.; Yin, X.; Que, W. Synergistically Coupling Phosphorus-Doped Molybdenum Carbide with MXene as a Highly Efficient and Stable Electrocatalyst for Hydrogen Evolution Reaction. ACS Sustainable Chem. Eng. 2020, 8, 12990—12998.
- (29) Chen, Y.-Y.; Zhang, Y.; Jiang, W. J.; et al. Pomegranate-like N,P-Doped Mo2C@C Nanospheres as Highly Active Electrocatalysts for Alkaline Hydrogen Evolution. ACS Nano 2016, 10, 8851–8860.
- (30) Jia, J.; Xiong, T.; Zhao, L.; et al. Ultrathin N-Doped Mo2C Nanosheets with Exposed Active Sites as Efficient Electrocatalyst for Hydrogen Evolution Reactions. ACS Nano 2017, 11, 12509–12518.
- (31) Anjum, M. A. R.; Lee, M. H.; Lee, J. S. Boron- and Nitrogen-Codoped Molybdenum Carbide Nanoparticles Imbedded in a BCN Network as a Bifunctional Electrocatalyst for Hydrogen and Oxygen Evolution Reactions. *ACS Catal.* **2018**, *8*, 8296–8305.
- (32) Ang, H.; Tan, H. T.; Luo, Z. M.; et al. Hydrophilic Nitrogen and Sulfur Co-doped Molybdenum Carbide Nanosheets for Electrochemical Hydrogen Evolution. *Small* **2015**, *11*, 6278–6284.
- (33) Tang, C.; Wang, W.; Sun, A.; et al. Sulfur-Decorated Molybdenum Carbide Catalysts for Enhanced Hydrogen Evolution. *ACS Catal.* **2015**, *5*, 6956–6963.
- (34) Wei, Z.; Hu, X.; Ning, S.; Kang, X.; Chen, S. Supported Heterostructured MoC/Mo2C Nanoribbons and Nanoflowers as Highly Active Electrocatalysts for Hydrogen Evolution Reaction. ACS Sustainable Chem. Eng. 2019, 7, 8458–8465.
- (35) Liu, C.; Sun, L.; Luo, L.; et al. Integration of Ni Doping and a Mo2C/MoC Heterojunction for Hydrogen Evolution in Acidic and Alkaline Conditions. ACS Appl. Mater. Interfaces 2021, 13, 22646—22654
- (36) Lin, H.; Shi, Z.; He, S.; et al. Heteronanowires of MoC-Mo2C as efficient electrocatalysts for hydrogen evolution reaction. *Chem. Sci.* **2016**, *7*, 3399–3405.
- (37) Liu, W.; Wang, X.; Wang, F.; et al. A durable and pH-universal self-standing MoC–Mo2C heterojunction electrode for efficient hydrogen evolution reaction. *Nat. Commun.* **2021**, *12*, No. 6776.
- (38) Chen, Y.; Gao, B.; Wang, M.; et al. Dual-phase MoC-Mo2C nanosheets prepared by molten salt electrochemical conversion of CO2 as excellent electrocatalysts for the hydrogen evolution reaction. *Nano Energy* **2021**, *90*, No. 106533.
- (39) Upadhyay, S.; Pandey, O. P. Synthesis of Mo2C/MoC/C nanocomposite for hydrogen evolution reaction. *J. Solid State Electrochem.* **2022**, *26*, 559–564.
- (40) Jeon, J.; Park, Y.; Choi, S.; et al. Epitaxial Synthesis of Molybdenum Carbide and Formation of a Mo2C/MoS2 Hybrid Structure via Chemical Conversion of Molybdenum Disulfide. *ACS Nano* **2018**, *12*, 338–346.
- (41) Jia, L.; Liu, B.; Zhao, Y.; et al. Structure design of MoS2@ Mo2C on nitrogen-doped carbon for enhanced alkaline hydrogen evolution reaction. *J. Mater. Sci.* **2020**, *55*, 16197–16210.
- (42) Zhao, Z.; Qin, F.; Kasiraju, S.; et al. Vertically Aligned MoS2/Mo2C hybrid Nanosheets Grown on Carbon Paper for Efficient Electrocatalytic Hydrogen Evolution. ACS Catal. 2017, 7, 7312–7318.
- (43) Zhang, K.; Zhao, Y.; Zhang, S.; et al. MoS2 nanosheet/Mo2C-embedded N-doped carbon nanotubes: synthesis and electrocatalytic hydrogen evolution performance. *J. Mater. Chem. A* **2014**, *2*, 18715–18719.

- (44) Yang, T. T.; Saidi, W. A. Graphene Activation Explains the Enhanced Hydrogen Evolution on Graphene-Coated Molybdenum Carbide Electrocatalysts. *J. Phys. Chem. Lett.* **2020**, *11*, 2759–2764.
- (45) Wan, C.; Leonard, B. M. Iron-Doped Molybdenum Carbide Catalyst with High Activity and Stability for the Hydrogen Evolution Reaction. *Chem. Mater.* **2015**, 27, 4281–4288.
- (46) Yu, F.; Gao, Y.; Lang, Z.; et al. Electrocatalytic performance of ultrasmall Mo2C affected by different transition metal dopants in hydrogen evolution reaction. *Nanoscale* **2018**, *10*, 6080–6087.
- (47) Chen, M.; Ma, Y.; Zhou, Y.; et al. Influence of Transition Metal on the Hydrogen Evolution Reaction over Nano-Molybdenum-Carbide Catalysts 2018, 8, No. 294.
- (48) Yang, T. T.; Saidi, W. A. Reconciling the Volcano Trend with the Butler–Volmer Model for the Hydrogen Evolution Reaction. *J. Phys. Chem. Lett.* **2022**, *13*, 5310–5315.
- (49) Yang, T. T.; Patil, R. B.; McKone, J. R.; Saidi, W. A. Revisiting trends in the exchange current for hydrogen evolution. *Catal. Sci. Technol.* **2021**, *11*, 6832–6838.
- (50) Nørskov, J. K.; Bligaard, T.; Logadottir, A.; et al. Trends in the Exchange Current for Hydrogen Evolution. *J. Electrochem. Soc.* **2005**, 152, J23–J26.
- (51) Sun, F.; Tang, Q.; Jiang, D.-e. Theoretical Advances in Understanding and Designing the Active Sites for Hydrogen Evolution Reaction. ACS Catal. 2022, 12, 8404–8433.
- (52) Wang, F.; Tian, X.; Jiao, H. Adsorption of CO, H2, H2O, and CO2 on Fe-, Co-, Ni-, Cu-, Pd-, and Pt-Doped Mo2C(101) Surfaces. *J. Phys. Chem. C* **2021**, *125*, 11419–11431.
- (53) Wang, T.; Liu, X.; Wang, S.; et al. Stability of  $\beta$ -Mo2C Facets from ab Initio Atomistic Thermodynamics. *J. Phys. Chem. C* **2011**, 115, 22360–22368.
- (54) Luo, Y.; Tang, L.; Khan, U.; et al. Morphology and surface chemistry engineering toward pH-universal catalysts for hydrogen evolution at high current density. *Nat. Commun.* **2019**, *10*, 269.
- (55) Nørskov, J. K.; Meulman, H.; Herder, J. et al. Trends in the Exchange Current for Hydrogen Evolution. *J. Electrochem. Soc. 152*, DOI: 10.1149/1.1856988 (2005).
- (56) Chase, M. W., Jr. NIST-JANAF Themochemical Tables. In J. Phys. Chem. Ref. Data, Monograph; 4th ed.; 1998; Vol. 9, pp 1–1951.
- (57) Caliskan, S.; Wang, A.; Qin, F.; House, S. D.; Lee, J.-K. Molybdenum Carbide-Reduced Graphene Oxide Composites as Electrocatalysts for Hydrogen Evolution. *ACS Appl. Nano Mater.* **2022**, *5*, 3790–3798.
- (58) Shi, X.-R.; Wang, S. G.; Wang, H.; et al. Structure and stability of  $\beta$ -Mo2C bulk and surfaces: A density functional theory study. *Surf. Sci.* **2009**, *603*, 852–859.
- (59) Mitchell, D. R. G. Circular Hough transform diffraction analysis: A software tool for automated measurement of selected area electron diffraction patterns within Digital Micrograph. *Ultramicroscopy* **2008**, *108*, 367–374.